Electroanalytical detection of heavy metals using metallophthalocyanine and silica-coated iron oxide composites

Denisha Gounden[1], Samson Khene[2], Nolwazi Nombona[3]*

[1]*School of Chemistry and Physics, University of KwaZulu-Natal, Durban, 4000, South Africa.*
[2]*Department of Chemistry, Rhodes University, Grahamstown, 6140, South Africa.*
[3]*Department of Chemistry, University of Pretoria, Pretoria, 0028, South Africa.*

*Corresponding author, e-mail: nolwazi.nombona@up.ac.za

Abstract

The monitoring of heavy metal ions particularly in water is important in safeguarding the environment and humans from the toxic effects these metal ions pose. This work describes the synthesis, characterization and electrocatalytic properties of silica coated iron oxide nanoparticles (Si-NP) in the presence of cobalt or iron phthalocyanines (MPc) for heavy metal (HM) detection. TEM, XRD, XPS and VSM confirmed the successful synthesis of Si-NP with an average diameter of 12.07 nm. The electrochemical sensing properties of MPc/Si-NP modified glassy carbon electrodes (GCE) were assessed for HM detection. Differential pulse anodic stripping voltammetry (DPASV) studies indicated detection limits that compared positively with literature. The FePc/Si-NP composite showed the lowest detection limits (S/N=3) of 3.66 μg L^{-1}, 11.56 μg L^{-1}, 2.28 μg L^{-1}, 4.54 μg L^{-1} for arsenic (As), cadmium (Cd), mercury (Hg) and lead (Pb), respectively. A linear working range of 10 – 100 μg L^{-1} was obtained for As^{3+}, Hg^{2+} and Pb^{2+} ions while it was between 20 - 100 μg L^{-1} for Cd^{2+} ions. Both composites displayed reproducible signals for the simultaneous detection of the HMs for 10 consecutive scans. These composites offer a cheap and simplistic sensing device for HM analysis.

Keywords: phthalocyanine, iron oxide, heavy metal detection.

Introduction

The detection of heavy metals (HMs) has been a subject of scientific research over the past years (Barakat 2011). Heavy metals such as As, Cd, Hg and Pb are major pollutants in aquatic environments as they are difficult to biodegrade and can easily accumulate in the human body via the food chain (Fu and Wang 2011; Moyo et al. 2011). Chronic exposure to HMs results in illnesses such as cancer and kidney failure (Jaerup 2003). Several methods including adsorption (Bao et al. 2016), chemical precipitation (Fu and Wang 2011), reverse osmosis (Mohsen-Nia et al. 2007) and membrane filtration (Landaburu-Aguirre 2010) have been used for the treatment and remediation of HMs in the environment. These treatment options however are often done on an industrial scale and incur large operational costs. The electrochemical detection of HMs marks an innovative and economically viable solution for wastewater

treatment (Yamada et al. 2008). Surface modification of electrodes with metal oxide nanoparticles such as cobalt oxide (Salimi et al. 2008), magnesium oxide (Wei et al. 2012) and nickel oxide (Wu et al. 2012) have gained considerable attention for the electrochemical detection of HMs due to their reported stability, large surface area and environmentally friendly nature. Amongst these metal oxides, iron oxide (Fe_3O_4) nanoparticles have sparked interest due to their ability to absorb toxic heavy metals in polluted water and their subsequent removal/recovery using high gradient magnetic separation (Laurent et al. 2008). When immobilized on electrode materials, these nanoparticles have been found to be effective for the electrochemical detection of HMs as they accumulate HMs on the surface of the electrode resulting in improved sensitivity(Yean et al. 2005; Neyaz et al. 2014; Yao et al 2014). Furthermore, Fe_3O_4 nanoparticles are cheap to synthesize when compared to gold (Au) nanoparticles or Au electrodes that have been previously used to detected $As^{3+/5+}$ and Hg^{2+} ions..

Iron oxides have hydroxy and oxygen groups with free electron pairs on their surface, which allows for strong coordination bonds with positively charged HMs (Fialova et al. 2014). The major drawback experienced during these interactions is insufficient sensitivity caused by the aggregation of iron oxide nanoparticles. To improve catalytic performance, iron oxide nanoparticles can be functionalized with silica to prevent nanoparticle aggregation, improve chemical stability and increase surface area for enhanced sensitivity (Andrade et al 2009;Liu et al. 2004; Wang et al. 2010). The silica coating is expected to further enhance sensitivity as it imparts a negative charge on the surface of the nanoparticles which is expected to increase the attractive force with positively charged HMs.). The functionalization of iron oxide nanoparticles with silica also prevents air oxidation which would destroy magnetisation. Particle size directly influences the adsorption capacity of the iron oxide nanoparticles.Particles less than 30 nm in diameter exhibit a large surface area and super paramagnetic properties (Cui et al. 2012).

Metallophthalocyanines (MPc) are considered valuable electrocatalysts because the ligands and electroactive metal centre behave as binding sites for HMs (Ceken et al. 2012). MPc redox processes are largely influenced by factors such as the solvent, metal centre and the nature of the substituents (Nyokong, 1995). MPcs carrying S, O and N atoms can form stable complexes with transition HM ions whilst the conductive nature of electroactive metals such as cobalt (Co) and iron (Fe) have shown to improve the catalytic performance of MPcs towards HM detection (Ceken et al. 2012).

In this study, we report for the first time (to our knowledge), the use of CoPc and FePc to enhance HM detection of silica coated iron oxide nanoparticles (Si-NP) on a glassy carbon

electrode. This composite displayed several advantages over other materials as it could be coated onto the GCE using the relatively simple but effective drop cast method, no pre-concentration steps were required and the Si-NPs were recoverable. This approach provides a sensitive and convenient method for the detection of HMs in aqueous solutions.

Experimental

Materials

Chemicals

Absolute ethanol, acetic anhydride (Ac_2O), acetone, 25% ammonia solution (NH_4OH), iron (III) chloride hexahydrate ($FeCl_3.6H_2O$), iron (II) chloride tetrahydrate ($FeCl_2.4H_2O$), formamide ($HCONH_2$), methanol (MeOH) and potassium carbonate (K_2CO_3) were obtained from Sigma Aldrich or Merck. Dimethylformamide (DMF) was obtained from Sigma Aldrich and dried using molecular sieves (5 Å) prior to use. Acetic acid, chloroform ($CHCl_3$), cobalt (II) acetate, 1,8-Diazabicyclo[5.4.0]undec-7-ene (DBU), 1-pentanol, high purity silica gel, Si gel TLC sheets, tetraethoxysilane (TEOS), sodium acetate, thionyl chloride ($SOCl_2$), 4-*tert*-butylphenol and heavy metal standards (1000 mg L^{-1}, TraceCERT® grade) of As, Cd, Hg and Pb were purchased from Sigma-Aldrich and used as received. 4-Nitrophthalonitrile was synthesised and purified according to literature (Young and Onyebuagu 1990). Deionized water with a conductivity of 15 $\mu S\ m^{-1}$ was used for the synthesis of iron oxide nanoparticles. Ultrapure water (5.5 $\mu S\ m^{-1}$) was used to make solutions for the electrochemical measurements. was obtained from a Milli-Q water purification system.

Equipment

Thin layer chromatography was performed on silica gel 60 F_{254} sheets. Column chromatography was achieved on silica gel 60 Å (63-200 μm). Ultraviolet/visible (UV/vis) absorption spectra were recorded on a Shimadzu UV-2250 spectrophotometer (Tokyo, Japan). Fourier transform infrared (FT-IR) spectra were obtained using a Perkin-Elmer Spectrum 100 FT-IR Spectrometer (Connecticut,USA) equipped with a diamond crystal ATR accessory. Mass spectroscopy was performed on a Bruker AutoFLEX III smart-beam MALDI-TOF mass spectrometer (Bremen, Germany) with an α-cyano-4-hydroxycinnamic acid matrix in the

positive ion mode. Transmission electron microscope (TEM) images were obtained using a JEOL JEM 1010 microscope (Boston, USA) operated at 100 kV. Digital images were captured using a 2k x 2k AMT CCD camera and were processed using Olympus Soft Imaging Solutions. Particle sizes were determined using iTEM Software by Soft Imaging Solutions. Scanning electron microscope (SEM) images and energy dispersive X-ray (EDX) spectra were obtained using a Zeiss Ultra Plus (Oberkochen, Germany) scanning electron microscope equipped with a field emission gun. EDX spectra were acquired using an Oxford X-Max detector with an 18 mm window and processed using AZtec Software by Oxford Instruments. X-ray diffraction (XRD) was carried out using a Rigaku MiniFlex 600 X-ray diffractometer (Texas, USA). The patterns were recorded at a scan speed of 4°/minute and processed using PDXL and Origin software. X-ray photoelectron spectroscopy (XPS) was performed using a Kratos Axis Ultra DLD (Manchester, UK) with an incident Al (monochromatic) anode, equipped with a charge neutraliser. The operating pressure was kept below 5 x10^{-9} Torr. For wide XPS scans, the following parameters were used: emission current was maintained at 10 mA and the anode (HT) voltage at 15 kV. The resolution used to obtain wide scans was at 80 eV pass energy using a hybrid lens in the slot mode. The centre used for the scans was at 590 eV, the width at 1205 eV with steps of 1 eV and dwell time of 100 ms. For high resolution scans, the resolution was changed to 80 eV pass energy in slot mode. The centre was at 402 eV and width at 12 eV for N (1s) with step size of 0.05 eV and dwell time of 500 ms. Magnetization measurements were recorded at room temperature using a LakeShore 735 vibrating sample magnetometer (VSM) (Ohio, USA). Electrochemical measurements were carried out on a 797 VA Computrace Electrochemical Workstation (Metrohm Instruments, Herisau, Switzerland). For these measurements a three electrode system was employed consisting of a platinum (Pt) wire auxiliary electrode, a Ag|AgCl pseudo reference electrode and a glassy carbon electrode (GCE) as the working electrode (3.0 mm). Ultrapure water was obtained from a Milli-Q water purification system (Molsheim, France). Conductivity tests of the heavy metals (concentration of 10 mg L^{-1}) were carried out in acetate buffer (pH 3.9).

Computational details

The geometry optimizations of the MPc---heavy metal were carried out by means of the UB3LYP density functional with the SDD basis set as applied in the Gaussian 03 software. The UB3LYP exchange–correlation density functional uses Becke's method via his B88 exchange functional and the Lee–Yang Parr correlation functional, which incorporates a combination of

semi-empirical Hartree–Fock and DFT exchange (Becke, 1993; Lee et al. 1988; Vosko et al. 1980; Stephens et al. 1994). The Gaussview 4.1 interface was employed for the visualizations of molecular orbitals (MOs) as well as other relevant properties.20.

Synthesis

Cobalt (II) Pc and iron (II) Pc (Figure 1) were synthesized according to previously reported procedures (Tau and Nyokong 2006).

CoPc - Yield: 0.52 g (52%). IR (ν_{max} cm^{-1}): 1229 (C-O-C); 1362 (CH$_3$); 1463, 1505, 1600 (C=C); 2866, 2903, 2956 (-C-H); 3038 (=C-H). UV-vis (CH$_3$Cl): λ_{max} nm (log ε): 672 (3.76); 605 (3.15); 326 (3.40). MS (MALDI-TOF) [M-H]$^+$ *m/z*: calculated 1166; found 1167.

FePc - Yield: 0.42 g (42 %.) IR (ν_{max} cm^{-1}): 1231 (C-O-C); 1363 (CH$_3$); 1469, 1506, 1601 (C=C); 2867, 2904, 2959 (-C-H); 3038 (=C-H). UV-vis (CH$_3$Cl): λ_{max} nm (log ε): 670 (3.76); 607 (3.22); 324 (3.47). MS (MALDI-TOF) [M-H]$^+$ *m/z*: calculated 1163; found 1164.
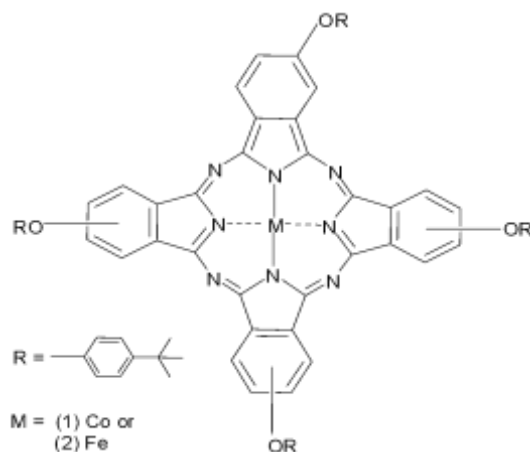

Fig. 1. Structure of 4β-(4-*tert*-butylphenoxy) cobalt (**1**) or iron (**2**) phthalocyanine.

Synthesis of iron oxide nanoparticles (NP) and silica coated iron oxide nanoparticles (Si-NP)

In a 250 mL round bottom flask, FeCl$_3$.6H$_2$O (4.40 g, 16.28 mmol) and FeCl$_2$.4H$_2$O (1.98 g, 9.96 mmol) were dissolved in deaerated deionized water (61 mL). The solution was left to stir for 30 minutes under nitrogen to prevent the oxidation of Fe^{2+} ions. Thereafter, NH$_4$OH (0.7 M, 143 mL) was added drop-wise and the solution was stirred for 10 minutes.

Upon the gradual addition of NH_4OH, the colour of the bulk solution changed from orange to dark brown and then black. The black iron oxide responded to a low gradient magnetic field. The NPs were washed twice with deionized water and stored as a suspension in deionized water (Shishehbore et al. 2011).

The NPs were coated with silica using a modified Stöber method (Shishehbore et al. 2011). The NP suspension was dispersed in absolute ethanol (74 mL) at 40 ℃. Sequentially, 25% NH_4OH (4 mL), deionized water (7.5 mL) and TEOS (20 mL) were added to the mixture. Maintaining the temperature, the mixture was stirred vigorously for 2 hours and sonicated for 1 hour. The nanoparticles were separated from the liquid via magnetic attraction and dispersed in absolute ethanol (30 mL). The coating procedure was repeated twice for the same NPs. The Si-NP were washed thrice with MeOH (30 mL) and separated from the liquid using magnetic attraction before being vacuum dried.

Electrode preparation and electrochemical measurements

Prior to modification, the bare glassy carbon electrode (GCE) was cleaned by successive sonication in HNO_3, absolute ethanol and Milli-Q water for 10 minutes. The GCE was then polished with alumina or diamond slurries and thoroughly rinsed with Milli-Q water. The modified electrode was prepared by drop casting CoPc or FePc (10 μL, 1.0 mM) in CH_3Cl onto the GCE surface. A uniform suspension of Si-NP (5.0 mg, 5 mL Milli-Q water) was then drop cast (10 μL) on the MPc modified electrode and was left to dry at room temperature for half an hour.

The bare and modified electrodes were characterized using 5 mM $K_3[Fe(CN)_6]$ in 1M KCl within a potential window of -1.5 V to 1.4 V at a scan rate of 100 mV s^{-1}. HM solutions were prepared by diluting HM standards in acetate or phosphate buffer to obtain varying concentrations of the target HM ions (10 μg L^{-1} to 100 μg L^{-1}). The HM analysis was carried out under optimised pH and deposition times (See Figures 11 and S5). Differential pulse anodic stripping voltammetry (DPASV) was used to electrochemically detect the individual HMs in solution as well as the for the simultaneous HM detection. The deposition potential for all DPASV measurements were -1.0 V and stripping was performed between -1.0 V to 1.0 V. The following parameters were used: frequency, 25 Hz; amplitude, 20 mV; increment potential 5 mV. All measurements were carried out at room temperature.

Results and discussion

Spectroscopic characterization of CoPc and FePc

The electronic absorption spectra of CoPc and FePc in CH_3Cl are shown in Fig. 2. The observed electronic absorption spectra is typical of Pc metal complexes (Mack and Kobayashi 2011). Intense single Q bands, due to the excitation from the highest occupied molecular orbital (HOMO, a_{1u}) to the lowest unoccupied molecular orbital (LUMO, e_g) is observed at 674 nm for both FePc and CoPc. The weak band appearing in the 710 nm region for the FePc is consistent with aggregation as it decreases upon dilution. The MPcs also exhibit typical B-bands between 320 nm - 326 nm corresponding to transitions from a_{2u} and b_{2u} to the e_g level (Mack and Kobayashi 2011). The bands appearing between the 370 – 400 nm region, for FePc, is due to metal to ligand charge transfer (Ceylan et al. 2015). However, for CoPcs the band in the 370 - 400 nm region is known not to correspond to charge transfer transition.
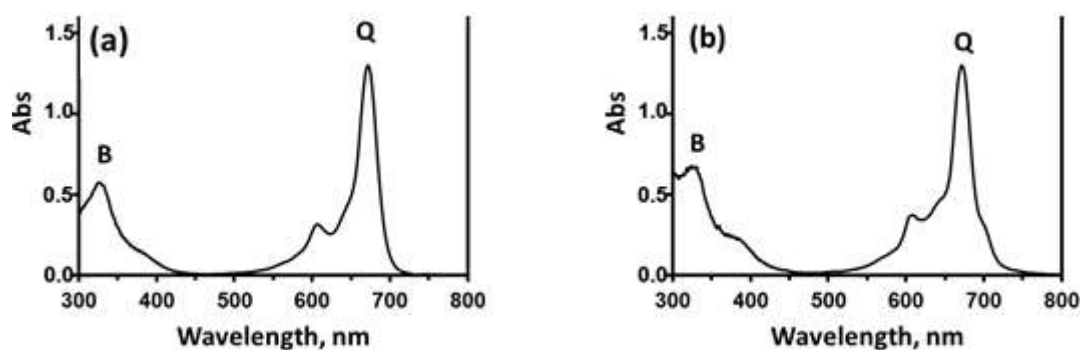

Fig. 2. Absorption spectrum of (a) CoPc and (b) FePc.

Synthesis and characterisation of NPs and Si-NPs

The Si-NP were prepared via a co-precipitation method and were functionalized with silica using a modified Stöber sol-gel method (Shishehbore et al. 2011). During the sol-gel process, TEOS is hydrolysed in the presence of a base to form silanol (Si-OH) which then undergoes a condensation reaction to produce a sol (Wu et al. 2008). The hydrolysis and condensation reactions take place simultaneously. The hydroxyl groups on the surface of the NP attack and displace the alkoxy groups of the silanol molecules, eventually forming covalent

bonds between silicon and oxygen (Si-O-Si) (Dave and Chopda 2014). The silica coating is used to prevent agglomeration of the NP as well as potential dissolution under acidic conditions (Haddad et al. 2004).

Transmission electron microscopy (TEM) and particle size distribution analysis

A TEM image of the Si-NP is shown in Fig. 3a. The NP and Si-NP are predominantly spherical and show some aggregation. The average particle size for the NP was determined to be approximately 5.03 nm in diameter, whilst Si-NP were approximately 12.07 nm in diameter (Fig. 3b). The increase in nanoparticle diameter for the Si-NP is attributed to the silica coating (Shishehbore et al. 2011).
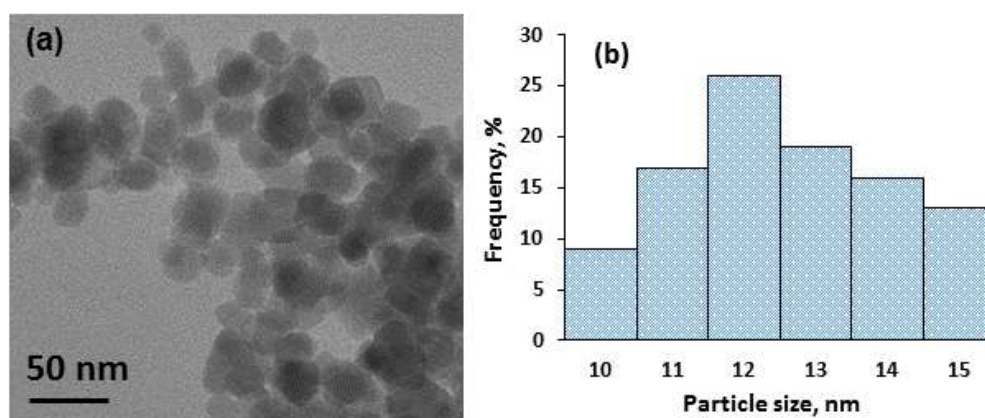

Fig. 3. (a) TEM image and (b) size distribution graph of Si-NP.

Scanning electron microscopy (SEM) and energy dispersive X-Ray spectroscopy (EDX)

The surface morphology of the NP was studied using SEM. The SEM images confirm that the NP and Si-NP have a spherical morphology of uniform size (Fig. 4a). Elemental analysis using EDX revealed the presence of Fe and O for the NPs and the presence of Si, Fe and O for the Si-NP (Fig. 4b). The Si-NP showed a relatively higher amount of Si (24 %) compared to the amount of Fe. The high Si content indicates that the Si-NP have a relatively thick silica coating on the surface.
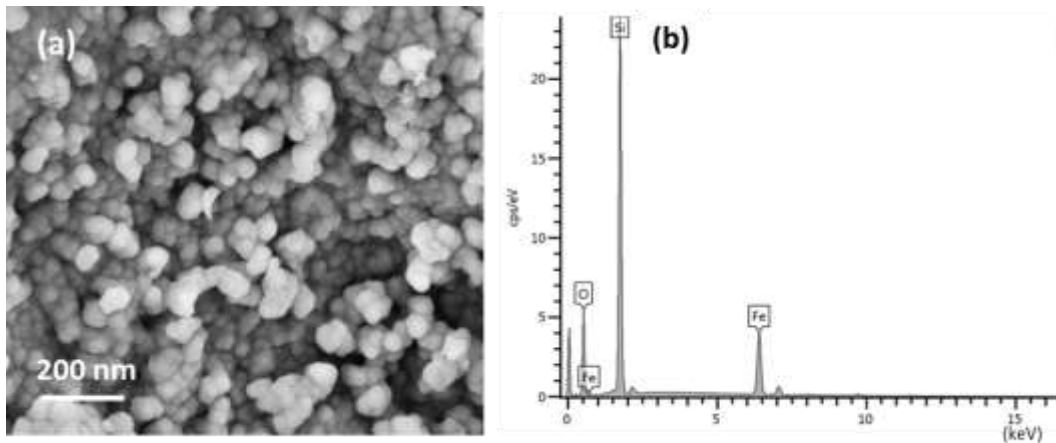
Fig. 4. (a) SEM images and (b) EDX spectrum of Si-NP.

Magnetic properties

The magnetic hysteresis of the NP and Si-NP is shown in Fig. 5. The insert shows an expanded window of the lower magnetic field of the hysteresis loop. The Si-NP display an s-shaped hysteresis curve indicating the superparamagnetic nature of the nanoparticles (Li et al. 2011). A similar curve was observed for the NP (Fig. 5a). The magnetic saturation (M_s) at the highest field of 14 000 Oe was 69.60 emu/g and 14.01 emu/g for the NP and Si-NP respectively. The Si-NP showed a decreased M_s compared to the NP due to the non-magnetic behaviour of the silica shell on the surface of the Si-NP (Mohammadi and Barikani 2014). The coercive fields (H_c), an indication of magnetic strength, was determined to be 13.37 Oe and 22.83 Oe for the NP and Si-NP respectively. These values indicate that both nanoparticles exhibit soft magnetic behaviour (Buschow 2013). The increased H_c for the Si-NP is due to increased particle size, large nanoparticles have an increased number of domains compared to smaller nanoparticles and this result in increased H_c (Sattler 2016).
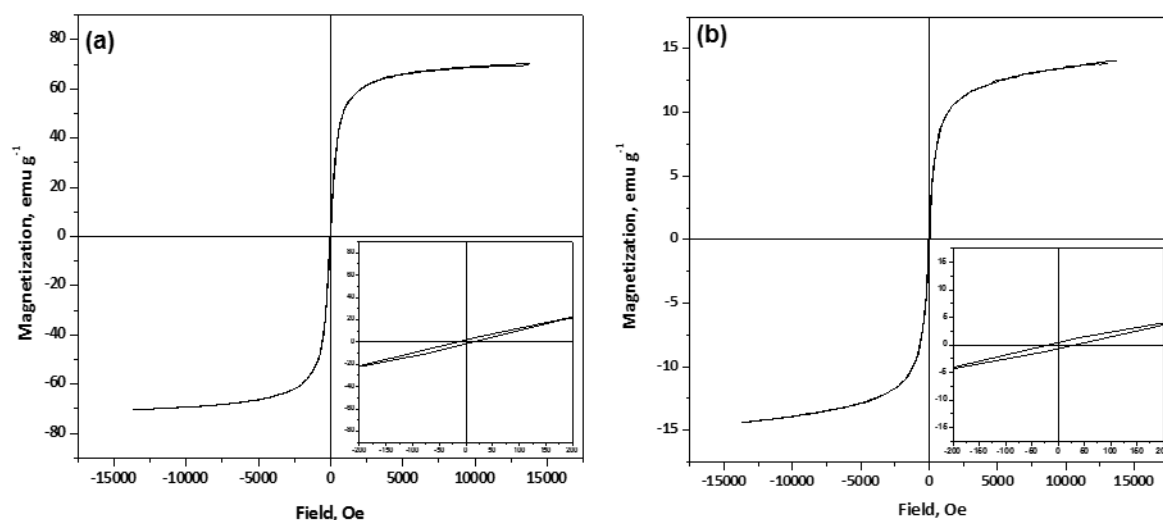
Fig. 5. Magnetometric curve for (a) NP and (b) Si-NP.

Fourier transform infrared spectroscopy (FTIR)

The chemical nature of the nanoparticles was evaluated using FT-IR. Fig. 6 shows the IR spectra of the NP and Si-NP. Absorption peaks for the NP (Fig. 6a) were observed at 432 cm^{-1}, 539 cm^{-1} and 1423 cm^{-1} corresponding to Fe-O stretching modes associated with the Fe^{2+} and Fe^{3+} ions in the octahedral and tetrahedral sites, respectively (Wu et al. 2010; Mahdavi et al. 2013; Lopez et al. 2010; Barilaro D, Baron et al. 2005). The Si-NP display bands at 563 and 1423 cm^{-1} correspond to the iron oxide core (Fig. 6b). The broad band appearing at 3186 cm^{-1} (O-H stretching mode) and the weaker band at 1619 cm^{-1} (O-H bending mode) observed in both spectra originate from trace amounts of adsorbed water on the surface of the nanoparticle and some residual NH_4OH (Lopez et al. 2010). The Si-O-Si asymmetric and symmetric peaks were observed at 1040 and 797 cm^{-1} for Si-NP (Fig. 6b) (Wu et al. 2010; Barilaro D, Baron et al. 2005; Ullah et al. 2014; Zhai et al. 2012). The functional groups identified in these spectra confirm the formation and coating of the Si-NP.
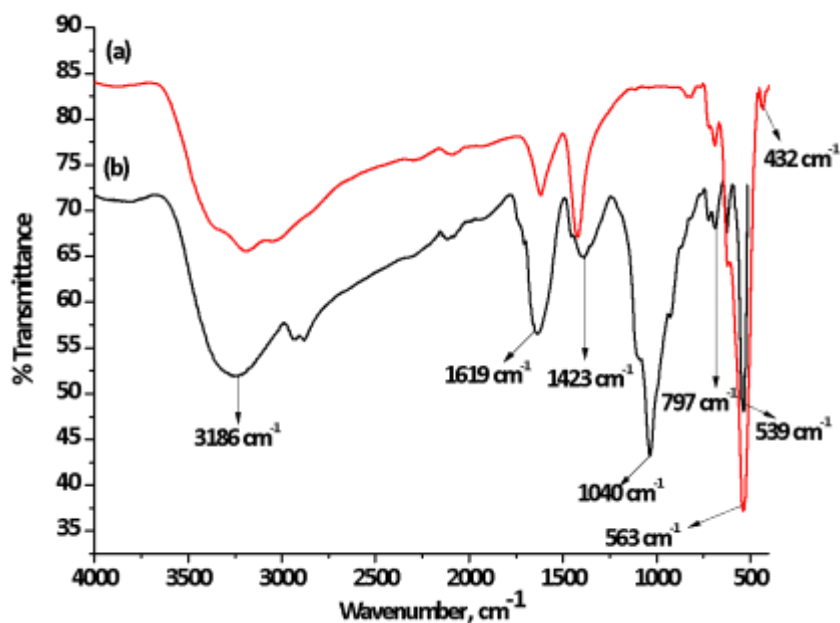
Fig. 6. IR spectra of (a) NP and (b) Si-NP.

X-ray photoelectron spectroscopy (XPS)

X-ray photoelectron spectroscopy was used to determine the chemical states of the nanoparticles. Fig. 7a shows the O 1s peak in the XPS spectrum for the NP. The bands at 529 and 531 eV are attributed to the lattice oxygen of the metal oxide and adsorbed OH$^-$ ions respectively (Cheng F et al. 2005; Pereira et al. 2010). The disappearance of the band at 531 eV (representing adsorbed OH$^-$ ions) for the Si-NP (Fig. 7b) suggests that the silica shell coats the magnetic core (Pereira et al. 2010).
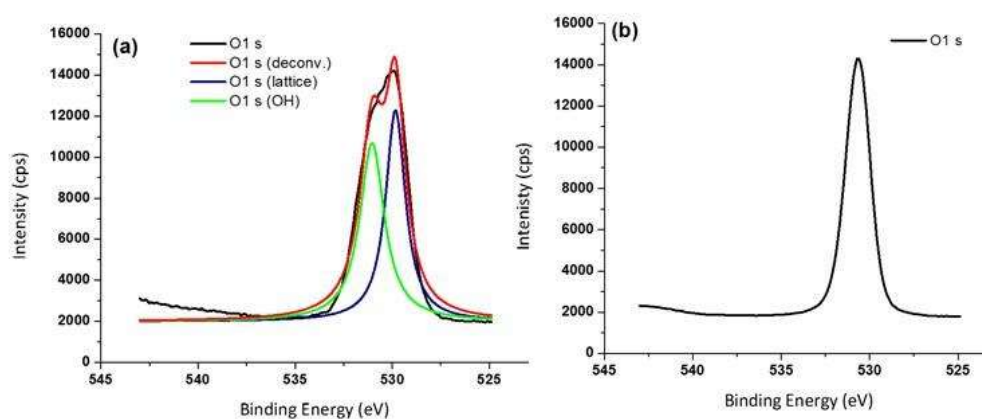

Fig. 7. O1 s peak in XPS spectrum for (a) NP and (b) Si-NP.

The Fe 2p region in the XPS spectrum for the NP is shown in Fig. 8a. An increase of an element's valence state leads to an increase in its bonding energy hence, the binding energy of Fe $2p_{3/2}$ was found to be larger for Fe^{3+} (~711 eV) compared to Fe^{2+} (~709 eV) (Pereira et al. 2010). The NP display a peak at 710.6 eV which lies between the reported 711 and 709 eV range, confirming the presence of Fe^{2+} and Fe^{3+} in the NP (Li et al. 2011). The Fe $2p_{1/2}$ peak shown at 724.7 eV is less intense than the Fe $2p_{3/2}$ peak due to spin–orbit (j–j) coupling (Fig. 8a). During the j-j coupling Fe $2p_{3/2}$ is degenerate in four states whilst Fe $2p_{1/2}$ is degenerate in two states leading to less intense peaks for Fe $2p_{1/2}$ (Li et al. 2011). Similar Fe 2p results were observed for Si-NP (Fig. 8b). The assignments for the O1 s and Fe 2p components agree with previous studies on iron oxide surfaces (Li P et al. 2011; Pereira et al. 2010). In the Si 2p region (Fig. 8b) a typical Si band at 102 eV was observed (Pereira et al. 2010).
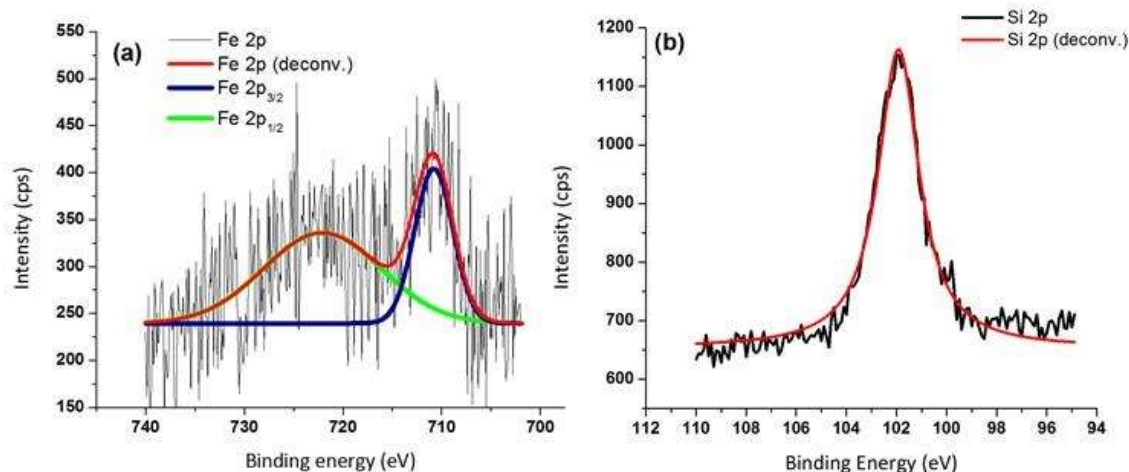

Fig. 8. Fe 2p peaks for (a) NP and (b) Si 2p for Si-NP in XPs spectra.

X-ray diffraction (XRD)

The crystallographic structure of the nanoparticles and composites were analysed by XRD. The XRD diffractograms for the NP (Fig. 9a) show peaks at 35.33° (220), 41.64° (311), 50.76° (400), 62.99° (422), 67.68° (511) and 74.61 ° (440). These peaks are consistent with the presence of the crystalline cubic spinel phase of magnetite (PC-PDF for magnetite (#110614)) (Yamashita and Hayes 2008; Ghandoor et al. 2012). Peaks at 26.73° (214) and 38.13° (226) are consistent with the presence of hematite (PC-PDF for hematite (#011053)) indicating that some of the magnetite (Fe_3O_4) nanoparticles were oxidized to hematite (α-Fe_2O_3) during synthesis. But XRD also indicates that magnetite is the predominant phase. Similar diffraction peaks can

be observed for the Si-NP, illustrating the stability of the crystalline phase of the iron oxide nanoparticles during the coating stages. The iron oxide peaks are of lower intensity for the Si-NP as compared to the NP. X-rays diffracted by the interior iron oxide core may have been absorbed by the layer of silica resulting in weakened diffraction peaks (Yu and Kwak 2010). The successful SiO_2 coating was confirmed by the presence of a new broad peak at a diffraction angle of approximately $2\theta = 25$ °, attributed to the amorphous silica shell. These results are in agreement with those reported in literature [14, 33, 34]. The average crystallite sizes of the nanoparticles were calculated using the Debye-Scherrer equation (1):

$$d = \frac{k\lambda}{\beta Cos\Theta} \tag{1}$$

where d is the particle size of the crystal, k is Sherrer constant, λ is the X-ray wavelength (0.15406 nm) for Cu K_α radiation, β is the peak width at half-height, and θ is the Bragg diffraction angle. The average crystallite sizes of the NP and Si-NP were calculated to be 6.17 nm and 10.90 nm and respectively which is in relatively good agreement with the average particle size determined by TEM.
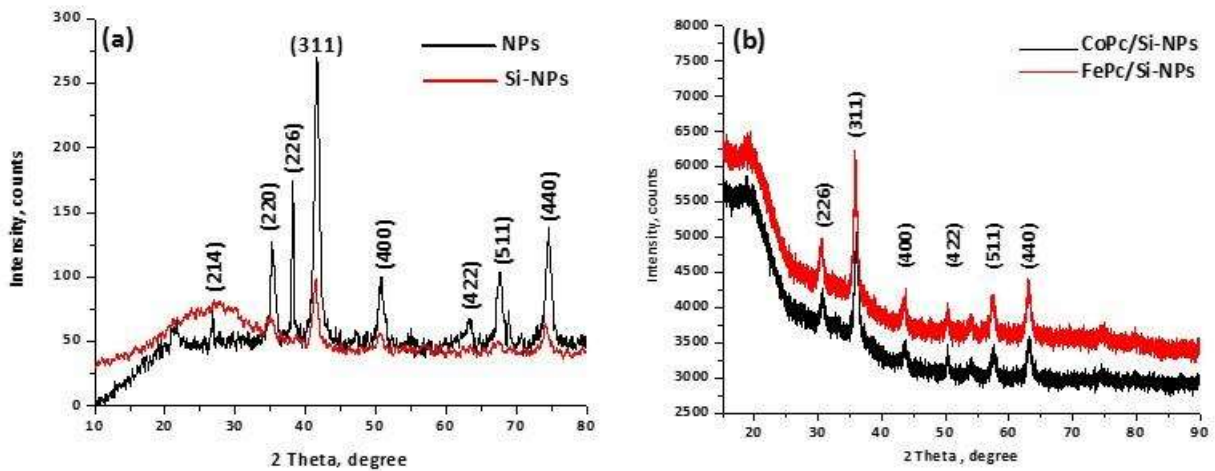

Fig. 9. XRD spectra of (a) NP and Si-NP and (b) CoPc/Si-NP and FePc/Si-NP.

The diffractograms of the CoPc/Si-NP and FePc/Si-NP are shown in Fig. 9b. Similar peaks relative to the NP and Si-NP were observed, however the peaks displayed higher intensity and were shifted towards lower 2θ values indicating a change to the lattice parameters of the nanoparticles, confirming the incorporation of the MPc (Chen and Li 2013; Berndt et al. (2001).

Electrode characterization

The electrocatalytic ability of the MPc/Si-NP composites were assessed on a GCE using cyclic voltammetry (CV) and ferricyanide as the redox probe. Fig. 10 shows the CV responses obtained for the bare and modified GCEs. The bare electrode shows the $[Fe(CN)_6]^{3-}/[Fe(CN)_6]^{4-}$ reversible couple with a peak-to-peak separation (ΔE_p) of 226 mV. Upon modification the CoPc/Si-NP and FePc/Si-NP modified electrodes showed a decreased ΔE_p of 151 and 141 mV respectively with slightly higher currents. The decreased ΔE_p values suggests better electron transfer experienced by the modified electrodes resulting in higher electron kinetics compared to the bare electrode. The $E_{1/2}$ values remained the same however slightly higher current density was observed on the modified electrodes indicating the conducting nature of the composite.
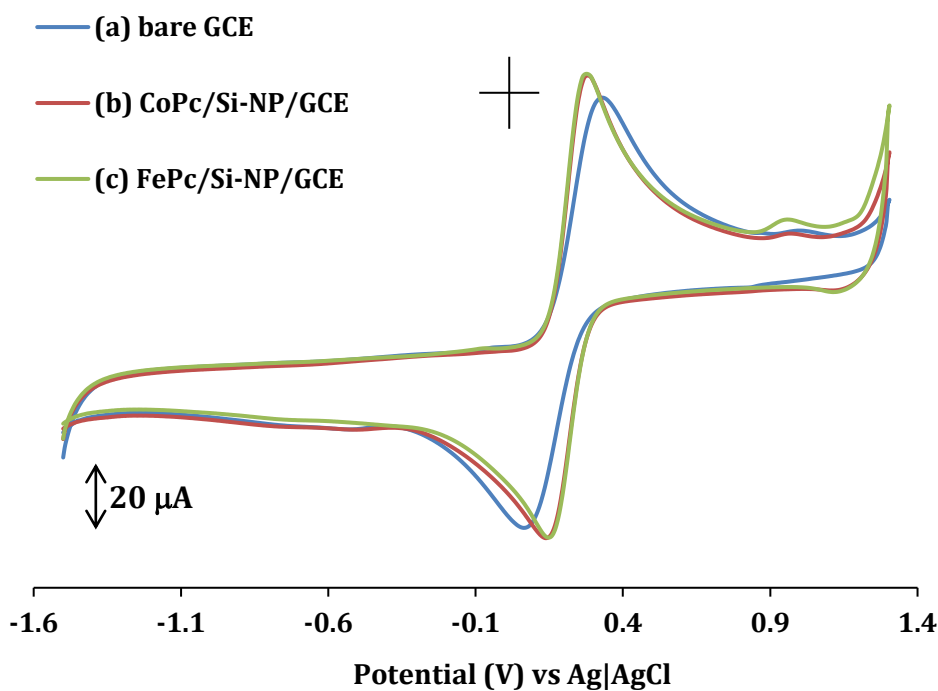

Fig. 10 CVs of (a) bare GCE, (b) CoPc/Si-NP/GCE and (c) FePc/Si-NP/GCE in 5 mM K$_3$[Fe(CN)$_6$] in 1M KCl. Scan rate: 100 mV s^{-1}.

The electroactive surface area (*A*) of the electrodes was determined for the bare and modified GCEs using the Randles-Sevcik equation (2):

$$I_p = 2.69 \times 10^5 \times A \times D^{\frac{1}{2}} \times n^{\frac{3}{2}} \times v^{\frac{1}{2}} C \qquad (2)$$

where I_p is the peak current (A), A the active surface area (cm^2), D the diffusion coefficient (cm^2 s^{-1}), n the number of electrons transferred in the redox reaction ($n = 1$) and v the scan rate (V s^{-1}). The measurements revealed that both modified electrodes have a larger electroactive surface area of 0.065 cm^2 when compared to the bare GCE which has a surface area of 0.040 cm^2. The larger surface area of the modified electrodes is expected to increase sensitivity towards HM detection.

Influence of pH and heavy metal ion concentration

The pH and deposition time were optimised to determine appropriate conditions for heavy metal detection. The effect of pH on the responses towards the HM ions is shown in Fig. 11 and the optimum pH's for the HM ions have been tabulated (Table 1). At pH > 4, current signals decreased for As^{3+} and Cd^{2+} ions due to the hydrolysis of these HMs at higher pHs (Zhu et al. 2014). Hydrolysed species may differ greatly from the free cations and can inhibit detection (Soleimani et al. 2008). The modified electrodes performed best at pH < 6, with FePc/Si-NP/GCE giving better peak current responses for all HMs compared to the CoPc/Si-NP/GCE. The effect of deposition time on the current response was also investigated (Supplementary Information). The optimum deposition time for all HMs was observed at 180 seconds.
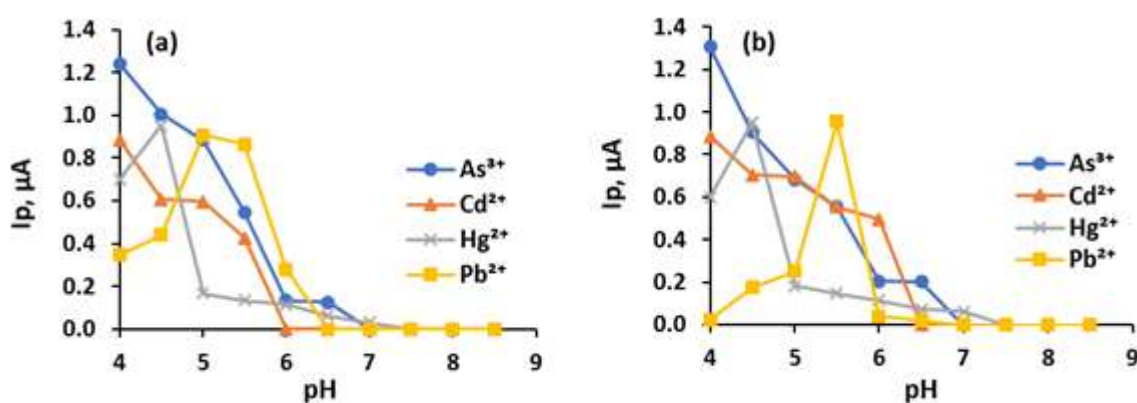

Fig. 11. Effect of pH on peak current on (a) CoPc/Si-NP and (b) FePc/Si-NP electrodes.

The DPASV responses of the composites towards HM detection were investigated for HM ion concentrations between 10 μg L^{-1} and 100 ug L^{-1} at optimum pH. Upon modification the individual As^{3+}, Cd^{2+}, Hg^{2+} and Pb^{2+} ions were detected at 0.02 V, -0.84 V, 0.04 V and -0.66 V for the CoPc/Si-NP composite and at 0.02 V, -0.82 V, 0.11 V and -0.65 V for the FePc/Si-NP composite respectively (See supplementary information). To serve as an example, Fig. 12 shows the DPASV response of Hg^{2+} on the CoPc/Si-NP/GCE and FePc/Si-NP/GCE with respective calibration plots for increasing Hg^{2+} concentrations. Both composites displayed a linear current increase as the HM concentration increased. A positive shift in the stripping peak potential was observed at high concentrations. According to the Nernst equation this is caused by the increase in the HM ion concentration on the electrode surface. This behaviour was observed for all HMs. A more complex stripping behaviour is observed at higher concentrations as noticeable shoulders were observed on the stripping peaks. The broadness is attributed to the greater accumulation of the HM ions which alters the surface of the electrode. Notably, FePc/Si-NP/GCE displayed larger peak current responses when compared to CoPc/Si-
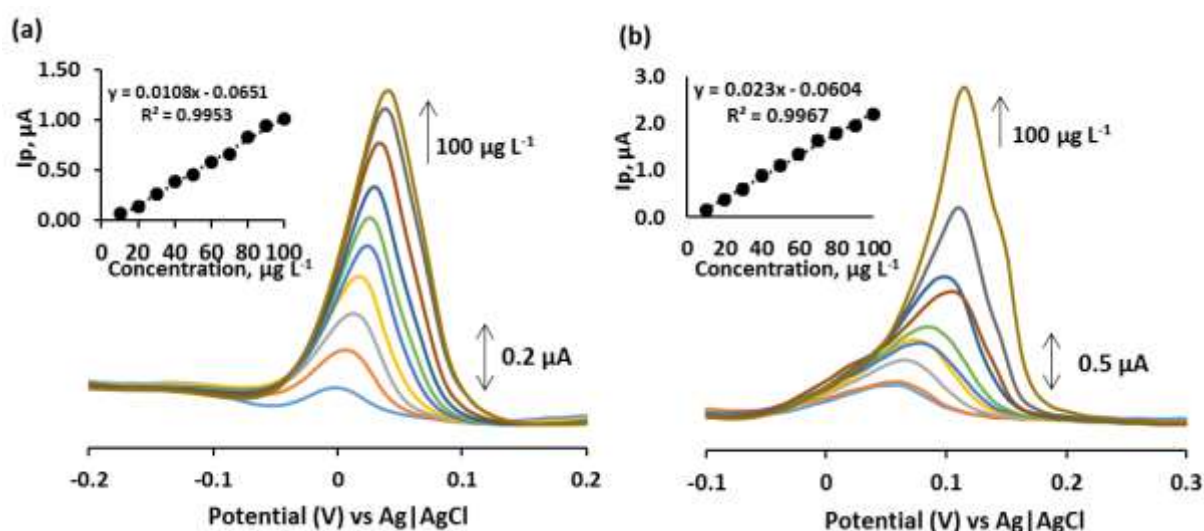
NP/GCE. However, the CoPc/Si-NP/GCE showed slightly better catalytic response for Hg^{2+}.

Fig. 12. DPASV curves and calibration plots for (a) CoPc/Si-NP/GCE and (b) FePc/Si-NP/GCE at varying concentrations of (10 μg L^{-1} – 100 μg L^{-1}) of Hg^{2+}. Deposition time: 180 s, deposition potential: -1.0 V, pH:4.5.

Table 1. Optimum pH for As^{3+}, Cd^{2+}, Hg^{2+} and Pb^{2+} on CoPc/Si-NP/GCE and FePc/Si-NP/GCE.

Metal	Composite	Optimum pH
Arsenic	CoPc/Si-NP	4.0
	FePc/Si-NP	4.0
Cadmium	CoPc/Si-NP	4.0
	FePc/Si-NP	4.0
Mercury	CoPc/Si-NP	4.5
	FePc/Si-NP	4.5
Lead	CoPc/Si-NP	5.0
	FePc/Si-NP	5.5

The limits of detection (LOD) were calculated based on a signal-to-noise ratio equivalent to three (S/N=3). The FePc/Si-NP composite showed the lowest LODs and the highest sensitivities for all HMs (Table 2). The sensitivity is highest for Hg for the FePc/Si-NP/GCE and follows the trend: $Hg^{2+} > Pb^{2+} > As^{3+} > Cd^{2+}$. The LODs also follow the same trend. The CoPc/Si-NP/GCE demonstrated sensitivity of the HMs in to the following order: $As^{3+} > Hg^{2+} = Pb^{2+} > Cd^{2+}$. Only As^{3+} and Hg^{2+} display LODs less than 5 µg L^{-1}. (See Supplementary Information for As^{3+}, Cd^{2+} and Pb^{2+} stripping responses).

Table 2 contains a comparison of the CoPc/Si-NP and FePc/Si-NP modified GCEs with previous electrochemical detection studies of As^{3+}, Cd^{2+}, Hg^{2+} and Pb^{2+}. Some of the mentioned methods achieve lower detection limits of the heavy metal ions however, it is noted that these methods have varying accumulation times and in some cases, may be longer than 180 s.

Table 2. Comparison of the performance of the proposed electrodes with other modified electrodes for the detection of As^{3+}, Cd^{2+}, Hg^{2+} and Pb^{2+} ions.

Sensor	Technique	Electrode	Metal Ion	LOD	Sensitivity	Reference
CoPc/Si-NP	DPASV	GCE	As^{3+}	4.39 µg L^{-1}	0.18 µA µg L^{-1}	present work
FePc/Si-NP	DPASV	GCE	As^{3+}	3.66 µg L^{-1}	0.20 µA µg L^{-1}	present work
Nano Au-CRV[1] film	DPV[2]	GCE	As^{3+}	15.58 µg L^{-1}	0.8075 µA µM^{-1} cm^2	Rajkumar et al. 2011
NPG[3]	ASV	Gold electrode	As^{3+}	1.499 µg L^{-1}	13.0 nA µM^{-1}	Jiang et al. 2015
CoPc/Si-NP	DPASV	GCE	Cd^{2+}	14.62 µg L^{-1}	0.10 µA µg L^{-1}	present work
FePc/Si-NP	DPASV	GCE	Cd^{2+}	11.56 µg L^{-1}	0.15 µA µg L^{-1}	present work
[4]Cr	SWASV[3]	CPE	Cd^{2+}	3.000 µg L^{-1}	-	Koudelkova et al. 2017
SnO_2 QDs[5]	CV	Gold electrode	Cd^{2+}	500.0 µg L^{-1}	77.5×10^2 nA ppm^{-1} cm^{-2}	Bhanjana et al. 2015
CoPc/Si-NP	DPASV	GCE	Hg^{2+}	4.890 µg L^{-1}	0.17 µA µg L^{-1}	present work
FePc/Si-NP	DPASV	GCE	Hg^{2+}	2.280 µg L^{-1}	0.37 µA µg L^{-1}	present work
Hg^{2+} IIP[6]	DPASV	CILE[6]	Hg^{2+}	20.06 µg L^{-1}	0.47 nM	Bahrami et al. 2015
MnPc	SWASV	GCE	Hg^{2+}	401.2 µg L^{-1}	1.45 A cm^{-2} M^{-1}	Çeken et al. 2012
CoPc/Si-NP	DPASV	GCE	Pb^{2+}	6.060 µg L^{-1}	0.17 µA µg L^{-1}	present work
FePc/Si-NP	DPASV	GCE	Pb^{2+}	4.540 µg L^{-1}	0.22 µA µg L^{-1}	present work
BRMCPE[7]	SWASV	CPE[8]	Pb^{2+}	15.00 µg L^{-1}	-	Devnani et al. 2014
MWCNT[9]	PSA[10]	CPE	Pb^{2+}	7.015 µg L^{-1}	-	Tarley et al. 2009

[1]CRV – crystal violet; [2]DPV - differential pulse voltammetry; [3]NPG – nano porous gold; [4]Cr – chromium (III) oxide; [5]QDs - quantum dots; [6]IIP - ion imprinted polymer; [7]BRMCPE - black rice; [8]CPE - carbon paste electrode; [9]MWCNT - multiwalled carbon nanotube; [10]PSA - potentiometric stripping analysis.

Simultaneous detection of heavy metal ions

The composites were tested for their ability to simultaneously detect the four HM ions in a mixed solution (1000 µg L^{-1}). Fig. 13 shows the stripping responses obtained for each composite in the mixture of HM ions at pH 4.5.
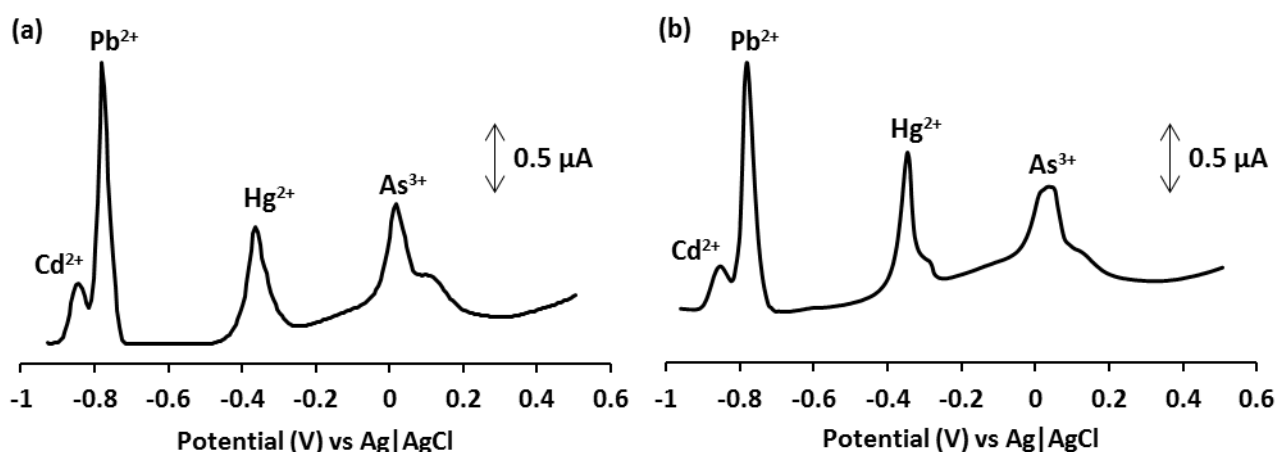

Fig. 13. Simultaneous HM detection on (a) CoPc/Si-NP/GCE and (b) FePc/Si-NP/GCE. Deposition time: 180 s, deposition potential: -1.0 V, pH:4.5.

The Pb^{2+} stripping current was significantly higher than those for the other metal ions for both composites and it also slightly overlaps with the Cd^{2+} peak (Fig. 13). This overlap may be due to interactions occurring between the deposited Cd^{2+} and Pb^{2+} ions or it may be due to competitive interactions arising from their similar atomic radii (Mohan and Pittman 2007; Turner 1987). The high currents observed for Pb^{2+} are attributed to Pb^{2+} being deposited more efficiently onto the electrode surface than Cd^{2+} (Mohan and Pittman 2007). There is a shift in the peak potential for Hg^{2+} (0.04 V to -0.35 V), Pb^{2+} (-0.66 V to -0.78 V) and Cd^{2+} (-0.84 V to -0.70 V) compared to the individual HM analysis whilst As^{3+} showed no significant change. This behaviour implies some interaction amongst the deposited metal ions (Manivannan et al. 2004). The As^{3+} stripping peak shows significant tailing and broadening particularly on the FePc/Si-NP/GCE. This is due to the strong complexing ability of iron oxide to As^{3+} (Feng et al. 2012; Jiang et al. 2012). Similar to the individual HM detection studies, the responses from the FePc/Si-NP/GCE were better than those obtained for the CoPc/Si-NP/GCE, indicating the FePc/Si-NP composite gives significantly better responses towards HMs than the CoPc/Si-NP composite. The peak currents of the metal ions decreased when detected simultaneously. This decrease could be attributed to the formation of an intermetallic compound of the HM ions

during the deposition process. The results suggest that there is a level of mutual interference even though the stripping peaks of the individual ions can be distinguished. The stability of the sensor was tested using the same electrode. The magnitude of the stripping current started to decrease after the tenth scan.

The interaction of CoPc with Pd, Cd, Hg and As was studied using DFT calculations. Fig. 14 shows the energy levels calculated for the interaction of CoPc with Pd, Cd and Hg. The LUMO (see supplementary results S8 and S9) also show substantial interaction exists between the analyte and the MPc. The LUMO of the CoPc-Pd and FePc-Pd had a different distribution compared to other MPc heavy metal interaction. Experimental results also show that Pd gives a much higher current compared to other metals. The DFT results suggests a similar interaction of the MPcs with heavy metals studied in this work. The above suggestion is based on the comparison of the HOMO energy level of the optimised MPc-heavy metal adduct, as shown in Figure 14 and S8 & 9. The theoretical results represent the energy changes as a result of the interaction. The DFT predicted energy changes do not agree with the experimental results. However, the negative DFT results suggest that the solvent condition plays an important role in the electrocatalysis of the analytes. The pH studies discussed above clearly show this strong dependence. The differences in analyte solvent interaction is demonstrated by the differences observed in the measured conductivity of the analytes in a solvent condition of pH 4.5 (See Supplementary information).
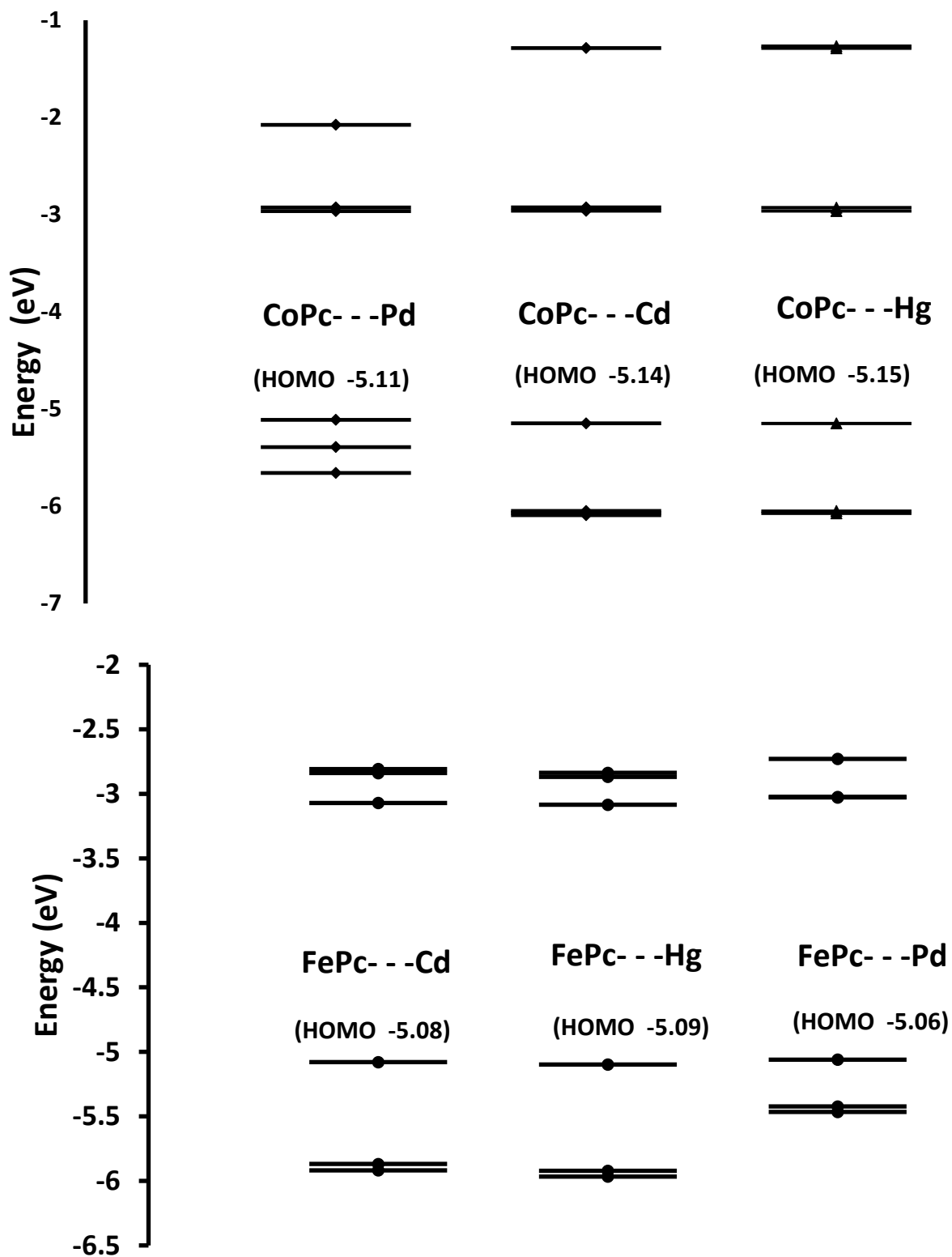
Fig. 14: Energy level diagram for the interaction of cobalt phthalocyanine with Pd, Cd, Hg and As. DFT calculations where done with B3LYP level of theory, using SDD basis sets.

Conclusions

This work investigated the applicability of MPc/Si-NP composites as materials for HM detection. A detailed account of the synthesis and characterization of the MPc and Si-NP material was reported. The composites displayed good electrochemical response to HMs with FePc/Si-NP/GCE showing a favourable response compared to the CoPc/Si-NP/GCE. The sensors also demonstrated simultaneous detection of HMs in solution. The composites displayed low LODs towards all HMs proving that they are suitable for monitoring trace amounts of HMs in trying to eliminate the persistence and toxicity of HMs in the environment.

Supplementary data

Table of contents

- **(i)** TEM and size distribution analysis of NP
- **(ii)** SEM and EDX of NP
- **(iii)** Cyclic voltammetry data of CoPc and FePc
- **(iv)** Optimisation of deposition time for DPASV
- **(v)** Analytical performance of CoPc/Si-NP/GCE
- **(vi)** Analytical performance of FePc/Si-NP/GCE
- **(vii)** Conductivity measurements of the HMs in acetate buffer, pH 4.1
- **(viii)** Molecular orbital modelling
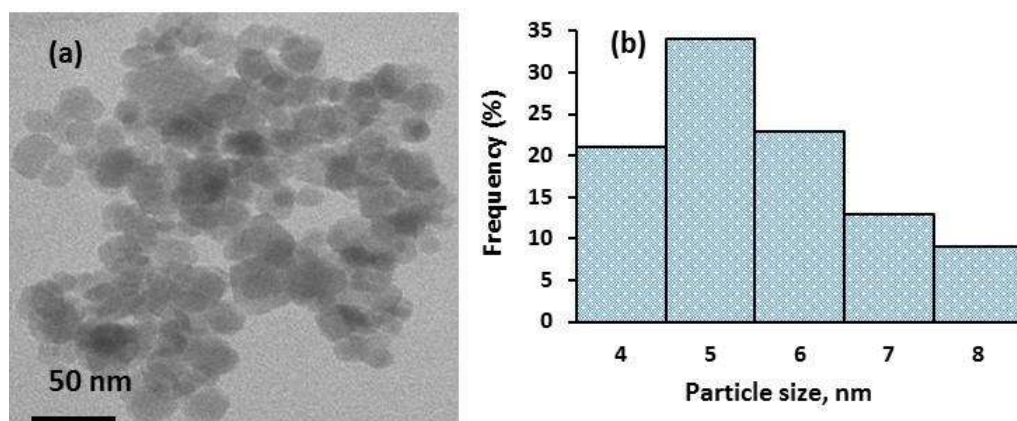
(i) TEM and size distribution analysis of NP

Figure S1: (a) TEM image and (b) particle size distribution of NP.
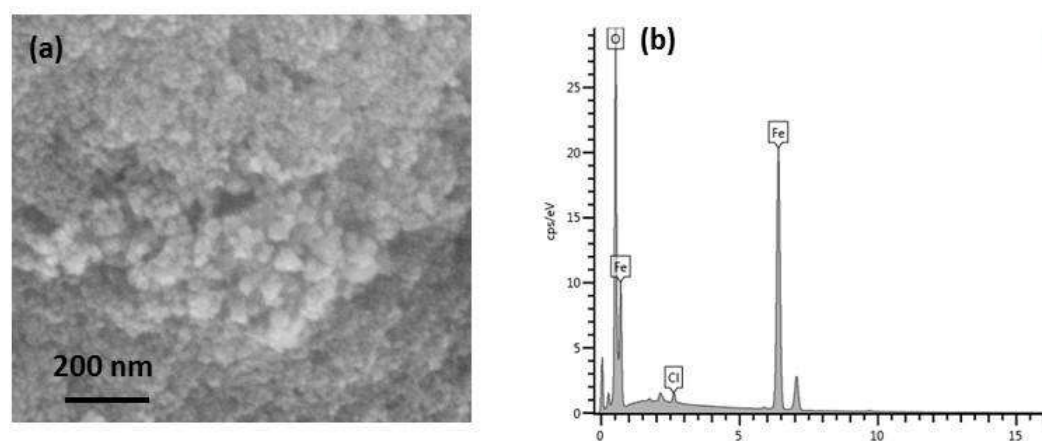
(ii) SEM and EDX of NP

Figure S2: (a) SEM image and (b) EDX of NP.

(iii) Cyclic voltammetry data of CoPc and FePc

Table S3.1: Redox potentials of Co and Fe Pcs in THF with 0.1 M TBABF$_4$ as supporting electrolyte.

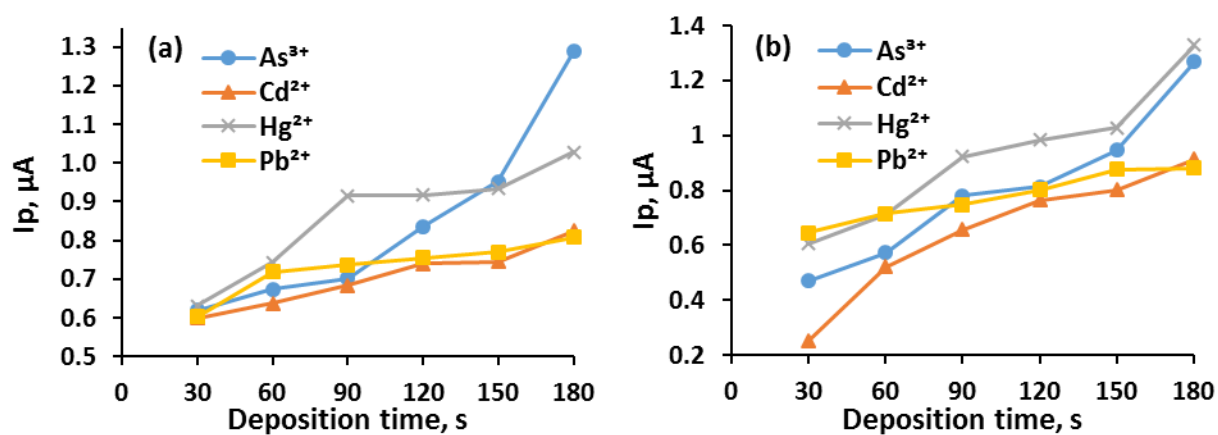| Complex		Process	ΔE, mV	E$_{1/2}$,V	Ip$_a$/Ip$_c$ (A)
CoPc	I	Co^{II}Pc^{-2}/ Co^{III}Pc^{-2}	56	+0.9	0.94
	II	Co^{III}Pc^{-2}/ Co^{III}Pc^{-1}	198	+0.2	0.50
	III	Co^{II}Pc^{-2}/ Co^{I}Pc^{-2}	115	-0.35	1.33
	IV	Co^{I}Pc^{-2}/ Co^{I}Pc^{-3}	147	-0.83	1.25
	V	Co^{I}Pc^{-3}/ Co^{I}Pc^{-4}	60	-1.36	1.06
FePc	I	Fe^{II}Pc^{-2}/ Fe^{III}Pc^{-2}	-	1.24	-
	II	Fe^{II}Pc^{-2}/ Fe^{I}Pc^{-2}	-	-0.27	-
	III	Fe^{I}Pc^{-2}/ Fe^{I}Pc^{-3}	-	-0.80	-
	IV	Fe^{I}Pc^{-3}/ Fe^{I}Pc^{-4}	-	-1.24	-

(iv)   Optimisation of deposition time for DPASV

Figure S5: Effect of deposition time on (a) CoPc/Si-NP and FePc/Si-NP.
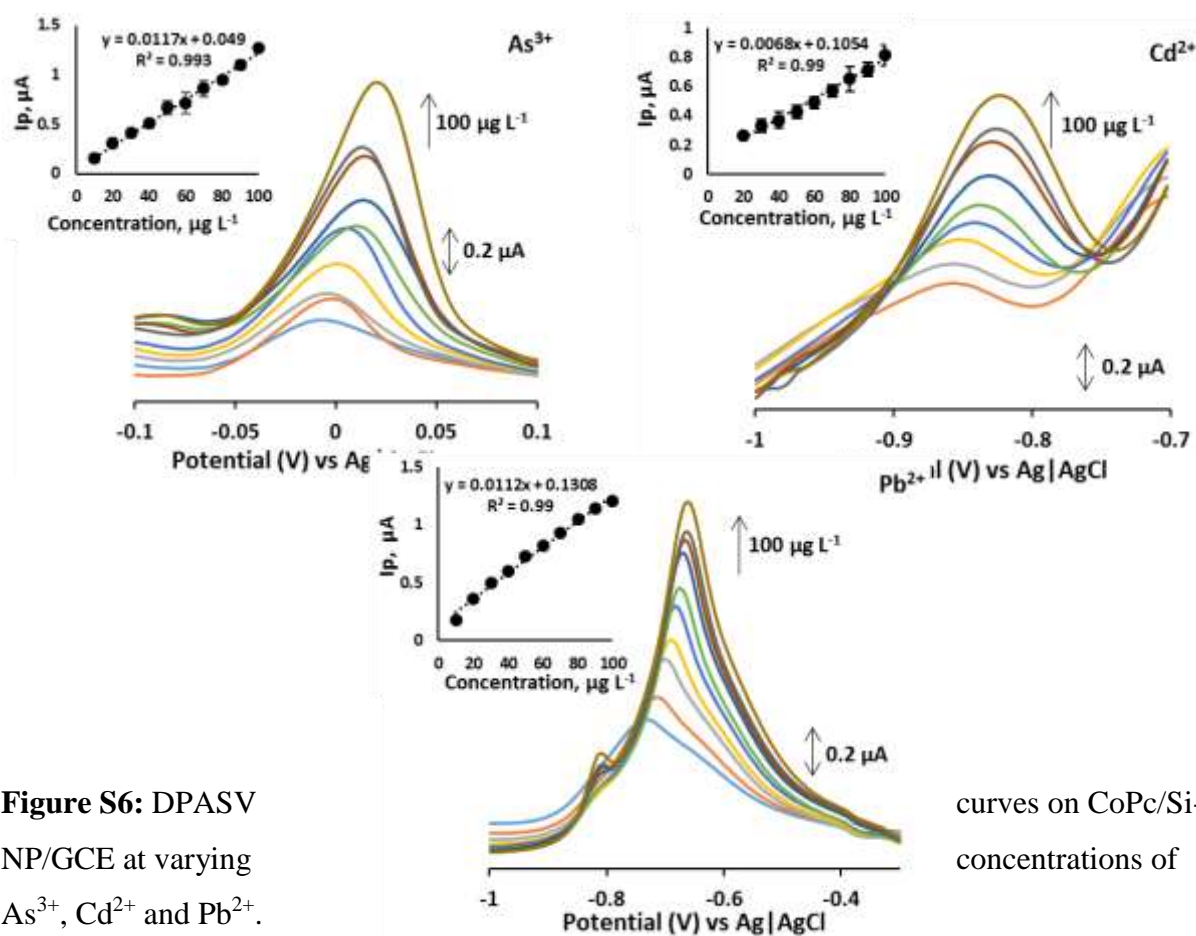
(v) Analytical performance of CoPc/Si-NP/GC

Figure S6: DPASV curves on CoPc/Si-NP/GCE at varying concentrations of As^{3+}, Cd^{2+} and Pb^{2+}.

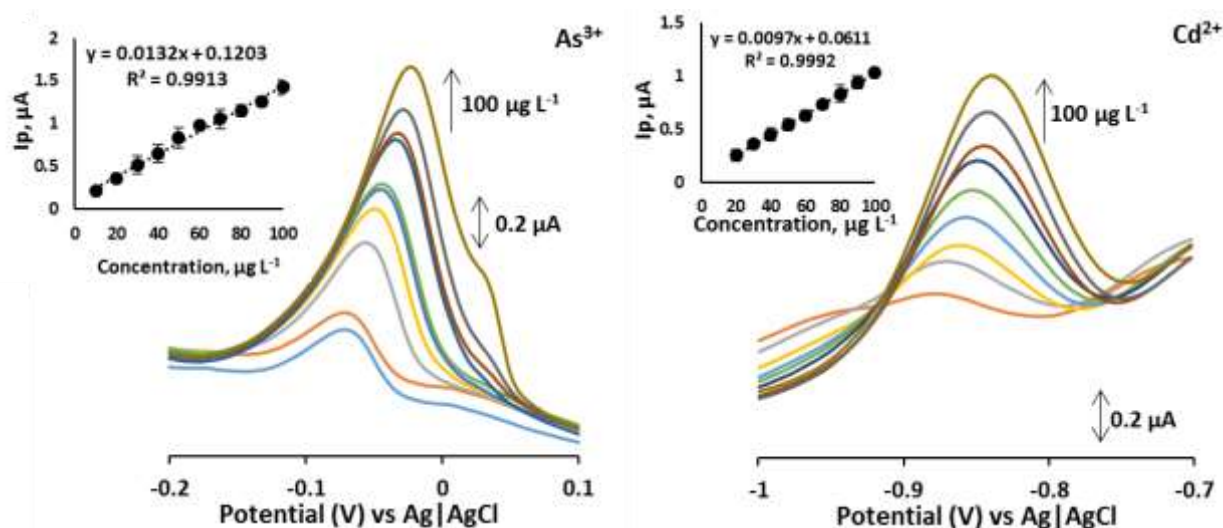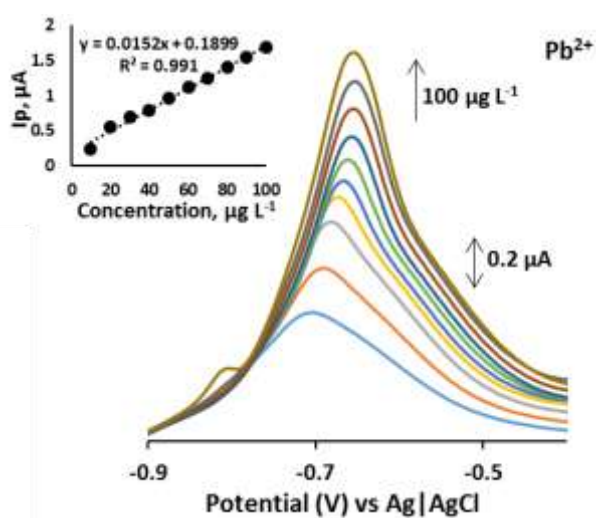**(vi) Analytical performance of FePc/Si-NP/GCE**

Figure S7: DPASV NP/GCE at varying As^{3+}, Cd^{2+} and Pb^{2+}. curves on FePc/Si-concentrations of

(vii) Conductivity measurements of the HMs in acetate buffer

Heavy Metal	Conductivity (mS cm^{-1})	
As^{3+}	2.79	
	2.82	
	2.80	
Average	2.803333333	As (2.803 ± 0.01527)
Standard Deviation	0.015275252	
Cd^{2+}	2.79	
	2.78	
	2.75	

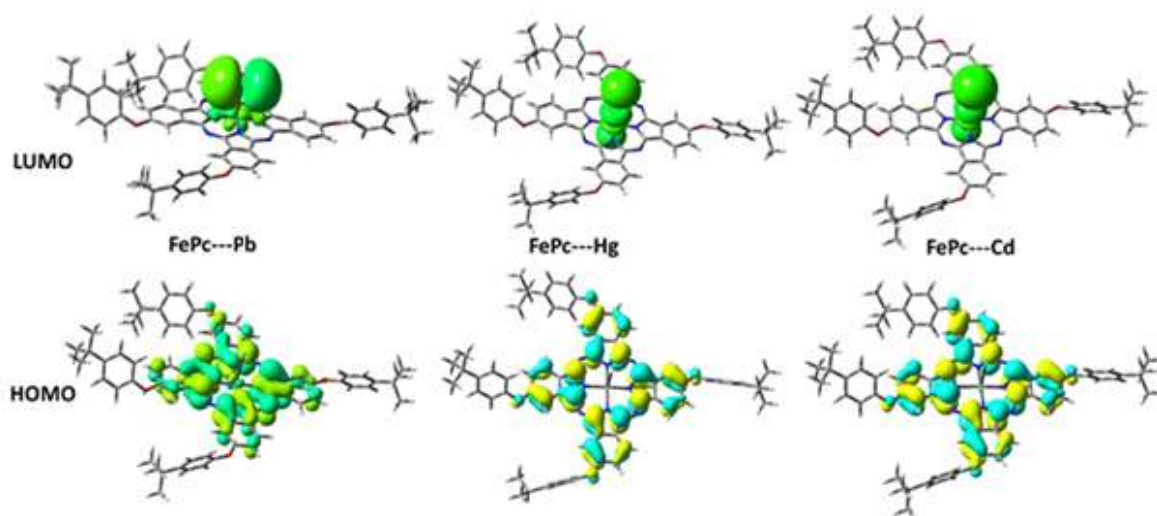|		
Average	2.773333333	Cd (2.773 ± 0.02082)
Standard Deviation	0.02081666	
Pb²⁺	2.86	
	2.87	
	2.84	
Average	2.856666667	Pb (2.857 ± 0.01527)
Standard Deviation	0.015275252	
Hg²⁺	3.37	
	3.37	
	3.36	
Average	3.366666667	Hg (3.367 0.05773)
Standard Deviation	0.005773503	

(viii) Molecular orbital modelling

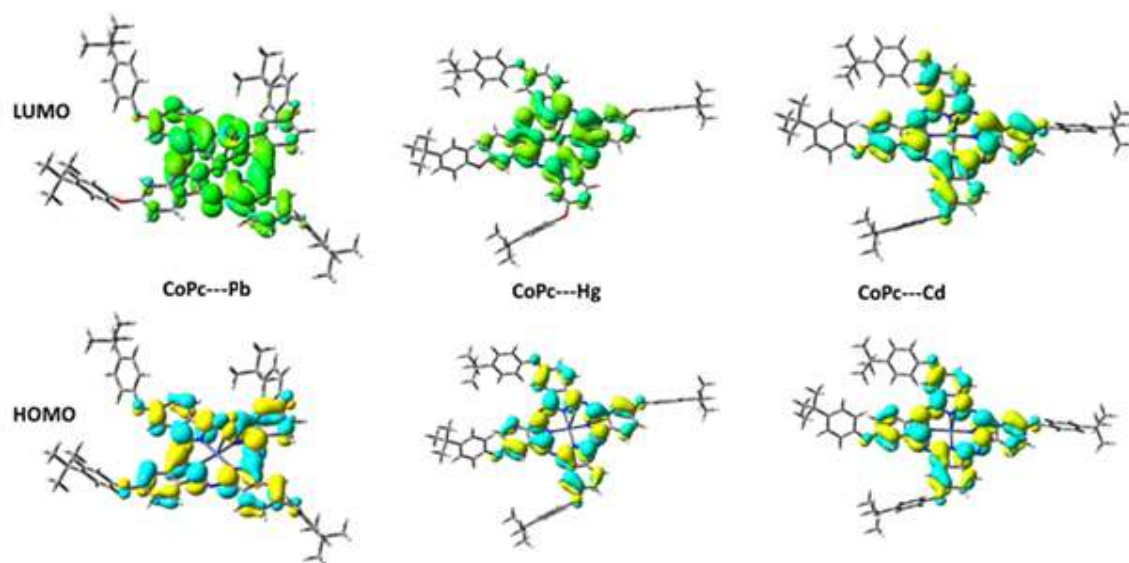**Figure S8**: HOMO and LUMO of FePc-HM

Figure S9: HOMO and LUMO of CoPc-HM

References

Andrade A.L, Souza DM, Pereira MC, Fabris JD, Domingues RZ, (2009) Synthesis and characterization of magnetic nanoparticles coated with silica through a sol-gel approach Cerâmica 55:420-424. doi.org/10.1590/S0366-69132009000400013

Barakat MA, (2011) New trends in removing heavy metals from industrial wastewater. Arabian Journal of Chemistry 4:361-377. doi.org/10.1016/j.arabjc.2010.07.019

Bahrami A, Besharati-Seidani A, Abbaspour A, Shamsipur M, (2015) A highly selective voltammetric sensor for nanomolar detection of mercury ions using a carbon ionic liquid paste electrode impregnated with novel ion imprinted polymeric nanobeads. Materials Science and Engineering: C 48: 205-212. doi.org/10.1016/j.msec.2014.12.005

Bao S, Li K, Ninga P, Peng J, Jin X, Tanga L, (2016) Highly effective removal of mercury and lead ions from wastewater by mercaptoamine-functionalised silica-coated magnetic nano-adsorbents: Behaviours and mechanisms. Applied Surface Science 393:457–466. doi.org/10.1016/j.apsusc.2016.09.098

Barilaro D, Barone G, Crupi V, Donato MG, Majolino D, Messina G, Ponterio R, (2005) Spectroscopic techniques applied to the characterization of decorated potteries from Caltagirone (Sicily, Italy). Journal of Molecular Structure 744:827–831. doi: 10.1016/j.molstruc.2004.11.083

Becke AD, (1993) Density-functional thermochemistry. III. The role of exact exchange The Journal of Chemical Physics 98:5648–5652. doi.org/10.1063/1.464913

Berndt CC, Khor KA, Lugscheider EF, (2001) Thermal Spray 2001: New Surfaces for a New Millennium; Proceedings of the 2nd International Thermal Spray Conference, 28-30 May 2001, Singapore. ASM International

Bhanjana G, Dilbaghi N, Kumar R, Umar A, Kumar S, (2015), SnO_2 quantum dots as novel platform for electrochemical sensing of cadmium. Electrochimica Acta 169: 97-102. doi.org/10.1016/j.electacta.2015.04.045

Buschow KHJ (2013) Handbook of Magnetic Materials, Elsevier, Great Britain, Oxford

Ceken B, Kandaz M, Koca A, (2012) Electrochemical metal-ion sensors based on a novel manganese phthalocyanine complex. Synthetic Metals 162:1524-1530. doi.org/10.1016/j.synthmet.2012.07.019

Ceylan N, Gümrükçü G, Karaoglan GK, Gül A, (2015) Synthesis, characterization, fluorescence spectra and energy transfer properties of a novel unsymmetrical zinc phthalocyanine with peripherally coordinated Ru(II) complex. Synthetic Metals 206:55-60. doi.org/10.1016/j.synthmet.2015.05.013

Chen L, Li J, (2013) A Study of γ-Fe_2O_3 Nanoparticles Modified Using $ZnCl_2$ during Synthesis. Advances in Materials Physics and Chemistry 3:31-35 doi: 10.4236/ampc.2013.31A004

Cheng F, Su C, Yang Y, Yeh C, Tsai C, Wu C, Wu M, Shieh D, (2005) Characterization of aqueous dispersions of Fe_3O_4 nanoparticles and their biomedical applications. Biomaterials 26:729–738. doi.org/10.1016/j.biomaterials.2004.03.016

Cui H, Yang W, Li X, Zhao H, Yuan Z, (2012) An electrochemical sensor based on a magnetic Fe_3O_4 nanoparticles and gold nanoparticles modified electrode for sensitive determination of

trace amounts of arsenic (III). Analytical Methods 4:4176-4181. doi.org/10.1039/C2AY25913C

Dave PN, Chopda LV, (2014) Application of Iron Oxide Nanomaterials for the Removal of Heavy Metals. Journal of Nanotechnology 1-14. doi.org/10.1155/2014/398569

Devnani, H, Rajawat D.S, Satsangee S.P, (2014) Black Rice Modified Carbon Paste Electrode for the Voltammetric Determination of Pb(II), Cd(II), Cu(II) and Zn(II). Springer (India) Proceedings of the National Academy of Sciences, India Section A: Physical Sciences 84: 361–370. https://doi.org/10.1007/s4001

Feng LY, Cao MH, Ma XY, Zhu YS, Hu CW, (2012) Superparamagnetic High-Surface-Area Fe_3O_4 Nanoparticles as Adsorbents for Arsenic Removal. Journal of Hazardous Material 217:439−446. doi: 10.1016/j.jhazmat.2012.03.073

Fu F, Wang Q (2011) Removal of heavy metal ions from wastewaters: A review, Journal of Environmental Management. 92:407-418. doi.org/10.1016/j.jenvman.2010.11.011

Ghandoor HE, Zidan HM, Khalil MMH Ismail MIM, (2012) Synthesis and Some Physical Properties of Magnetite (Fe_3O_4) Nanoparticles. International Journal of Electrochemical Science, **7**:5734 – 5745.

Guo X, Yun Y, Shanov VN, Halsall HB, Heineman WR, (2011) Determination of Trace Metals by Anodic Stripping Voltammetry Using a Carbon Nanotube Tower Electrode. Electroanalysis, 23:1252 – 1259. doi: 10.1002/elan.201000674

Haddad PS, Duarte EL, Baptista MS, Goya GF, Leite CAP, Itri R, (2004) Synthesis and characterization of silica-coated magnetic nanoparticles. Surface and Colloid Science 128:232-238. doi.org/10.1007/b97092

Jaerup L, (2003) Hazards of heavy metal contamination. British Medical Bulletin 68:167-182. doi.org/10.1093/bmb/ldg032

Jiang W, Chen XB, Niu YJ, Pan BC, (2012) Spherical Polystyrene-Supported Nano-Fe_3O_4 of High Capacity and Low-Field Separation for Arsenate Removal from Water. Journal of Hazardous Material 243:319−325. doi.org/10.1016/j.jhazmat.2012.10.036

Jiang J, Holm N, O'Brien K, (2015) Improved anodic stripping voltammetric detection of arsenic (III) Using nanoporous gold microelectrode. ECS Journal of Solid State Science and Technology, 4(10): S3024-S3029. doi: 10.1149/2.0061510jss

Koudelkova Z, Syrovy T, Ambrozova P, Moravec Z, Kubac L, Hynek D, Richtera L, Adam V, (2017) Determination of Zinc, Cadmium, Lead, Copper and Silver Using a Carbon Paste Electrode and a Screen-Printed Electrode Modified with Chromium(III) Oxide. Sensors (Basel, Switzerland) 17(8):1832 -1846. doi:10.3390/s17081832.

Laurent S, Forge D, Port M, Roch A, Robic C, Vander Elst L, Muller RN, (2008) Magnetic iron oxide nanoparticles: Synthesis, stabilization, vectorization, physico-chemical characterizations and biological applications, Chemical Reviews 108:2064-2110. doi: 10.1021/cr068445e

Landaburu-Aguirre J, Pongrácz E, Perämäki P, Keiski RL, (2010) Micellar-enhanced ultrafiltration for the removal of cadmium and zinc: Use of response surface methodology to improve understanding of process performance and optimization. Journal of Hazardous Materials. 180:524–534. doi.org/10.1016/j.jhazmat.2010.04.066

Lee C, Yang W, Parr RG, (1988) Development of the Colle-Salvetti correlation-energy formula into a functional of the electron density. Physical Review B 37:785–789. doi.org/10.1103/PhysRevB.37.785

Li P, Jiang EY, Bai HL, (2011) Fabrication of ultrathin epitaxial γ-Fe_2O_3 films by reactive sputtering. Journal of Physics D: Applied Physics 44:075003-075008. doi:10.1088/0022-3727/44/7/075003

Liu X, Ma Z, Xing J, Liu H, (2004) Preparation and characterization of amino–silane modified superparamagnetic silica nanospheres. Journal of Magnetism and Magnetic Materials 270:1-6. doi.org/10.1016/j.jmmm.2003.07.006

Lopez JA, González F, Bonilla FA, Zambrano G, Gómez ME, (2010) Synthesis and characterization of Fe_3O_4 magnetic nanofluid. Revista Latinoamericana de Metalurgiay Materiales 30:60-66.

Mack J, Kobayashi N, (2011) Low Symmetry Phthalocyanines and Their Analogues. Chemical Reviews 111:281-321. **doi:**10.1021/cr9003049

Mahdavi M, Ahmad MB, Haron M.J, Gharayebi Y, Shameli K, Nadi B, (2013) Fabrication and characterization of SiO_2/(3-Aminopropyl) triethoxysilane-coated magnetite nanoparticles for lead (II) removal from aqueous solution. Journal of Inorganic and Organometallic Polymers and Materials 23:599–607. doi:10.1007/s10904-013-9820-2

Manivannan A, Kawasaki R, Tryk DA, Fujishima A, (2004) Interaction of Pb and Cd during anodic stripping voltammetric analysis at boron-doped diamond electrodes. Electrochimica Acta 49:3313–3318. doi.org/10.1016/j.electacta.2004.03.004

Mohammadi A, Barikani M, (2014) Synthesis and characterization of superparamagnetic Fe_3O_4 nanoparticles coated with thiodiglycol. Materials Characterization 90:88-93. doi.org/10.1016/j.matchar.2014.01.021

Mohan D, Pittman CU, (2007) Arsenic removal from water/wastewater using adsorbents—A critical review. Journal of Hazardous Materials 142:1-53. doi.org/10.1016/j.jhazmat.2007.01.006

Mohsen-Nia M, Montazeri P, Modarress H, (2007) Removal of Cu^{2+} and Ni^{2+} from wastewater with a chelating agent and reverse osmosis processes. Desalination 217:276–281. doi.org/10.1016/j.desal.2006.01.043

Moyo S, Mujuru M, McCrindle RI, Mokgalaka-Matlala N, (2011) Environmental implications of material leached from coal. Journal of Environmental Monitoring 13:1488-1494.

Neyaz N, Siddiqui WA, Nair KK, (2014) Application of surface functionalized iron oxide nanomaterials as nanosorbents in extraction of toxic heavy metals from ground water: A review. International Journal of Environmental Sciences 4:472-483. doi: 10.6088/ijes.2014040400004

Nyokong T, (1995) Electrochemistry of some second-row transition-metal phthalocyanine complexes. South African Journal of Chemistry 48:23-29.

Pereira C, Pereira AM, Quaresma P, Tavares PB, Pereira E, Aráujo JP, Freire C, (2010) Superparamagnetic γ-Fe_2O_3@SiO_2 nanoparticles: a novel support for the immobilization of [$VO(acac)_2$]. Dalton Transactions 39:2842–2854. doi: 10.1039/B920853D

Sattler KD, (2016) Handbook of Nanophysics: Nanoparticles and Quantum Dots, CRC Press, Florida

Rajkumar M, Thiagarajan S, Chen S, (2011) Electrochemical Detection of Arsenic in Various Water Samples. International Journal of Electrochemical Sciences 6: 3164 – 3177.

Sergeyev S, Pouzet E, Debever O, Levin J, Gierschner J, Cornil J, Aspe RG, Geerts Y H, (2007) Liquid crystalline octaalkoxycarbonyl phthalocyanines: design, synthesis, electronic structure, self-aggregation and mesomorphism. Journal of Materials Chemistry 17: 1777–1784. doi:10.1039/B617856A

Shishehbore MR, Afkhami A, Bagheri H, (2011) Salicylic acid functionalized silica-coated magnetite nanoparticles for solid phase extraction and preconcentration of some heavy metal ions from various real samples. Chemistry Central Journal 5:1-10. doi: 10.1186/1752-153X-5-41

Soleimani F, Aghaiel H, Gharib F, (2008) Hydrolysis of cadmium cation in different ionic strength. Journal of Physical and Theoretical Chemistry 5:73-78

Stephens PJ, Devlin FJ, Chabalowski CF, Frisch M.J, (1994) Ab initio calculation of vibrational absorption and circular dichroism spectra using density functional force fields. The Journal of Physical Chemistry 98:11623–11627. doi:10.1021/j100096a001

Tarley C.R.T, Santos V.S, Baêta B.E.L, Pereira A.C., Kubota L.T, (2009) Simultaneous determination of zinc, cadmium and lead in environmental water samples by potentiometric stripping analysis (PSA) using multiwalled carbon nanotube electrode. Journal of Hazardous Materials 169: 256–262. doi.org/10.1016/j.jhazmat.2009.03.077

Tau P, Nyokong T, (2006) Synthesis and electrochemical characterisation of α- and β- tetra-substituted oxo(phthalocyaninato) titanium(IV) complexes. Polyhedron 25:1802–1810. doi.org/10.1016/j.poly.2005.11.025

Turner DR, (1987) Speciation and cycling of arsenic, cadmium, lead and mercury in natural waters, Lead, mercury, cadmium and arsenic in the environment, SCOPE, John Wiley & Sons Ltd, New York

Vosko SH, Wilk L, Nusair M, (1980) Accurate spin-dependent electron liquid correlation energies for local spin density calculations: a critical analysis. Canadian Journal of Physics 58:1200–1211. doi.org/10.1139/p80-159

Wang J, Zheng S, Shao Y, Liu J, Xu Z, Zhu D, (2010) Amino-functionalized $Fe_3O_4@SiO_2$ core–shell magnetic nanomaterial as a novel adsorbent for aqueous heavy metals removal. Journal of Colloid and Interface Science 349:293-299. doi.org/10.1016/j.jcis.2010.05.010

Wu W, Q. He and C. Jiang, (2008) Magnetic Iron Oxide Nanoparticles: Synthesis and Surface Functionalization Strategies. Nanoscale Research Letters 3:397–415. doi: 10.1007/s11671-008-9174-9

Wu W, Xiao XH, Zhang SF, Peng TC, Zhou J, Ren F, Jiang CZ, (2010) Synthesis and Magnetic Properties of Maghemite γ-Fe_2O_3 Short-Nanotubes. Nanoscale Research Letters 5:1474–1479. doi: 10.1007/s11671-010-9664-4

Yamada D, Ivandini TA, Komatsu M, Fujishima A, Einaga Y, (2008) Anodic stripping voltammetry of inorganic species of As^{3+} and As^{5+} at gold-modified boron doped diamond electrodes. Journal of Electroanalytical Chemistry 615:145–153. doi.org/10.1016/j.jelechem.2007.12.004

Yamashita T, Hayes P, (2008) Analysis of XPS spectra of Fe^{2+} and Fe^{3+} ions in oxide materials. Applied Surface Science 254:2441–2449. doi.org/10.1016/j.apsusc.2007.09.063

Yao X-Z, Guo Z, Yuan Q-H, Liu Z-G, Liu J-H, Huang X-J, (2014) Exploiting differential electrochemical stripping behaviors of Fe_3O_4 nanocrystals toward heavy metal ions by crystal cutting. Applied Materials & Interfaces 6:12203−12213 doi.org/10.1021/am501617a

Yean S, Cong L, Yavuz CT, Mayo JT, Yu WW, (2005) Effect of magnetite particle size on adsorption and desorption of arsenite and arsenate. Journal of Materials Research 20:3255-3264. doi: 10.1557/jmr.2005.0403

Young JG, and Onyebuagu W, (1990) Synthesis and characterization of di-disubstituted phthalocyanines. The Journal of Organic Chemistry 55:2155–2159. doi/abs/10.1021/jo00294a032

Yu BY, Kwak S, (2010) Assembly of Magnetite Nanoparticles into Spherical Mesoporous Aggregates with a 3-D Wormhole-Like Porous Structure. Journal of Materials Chemistry 20:8320-8328. doi: 10.1039/c0jm01274b

Zhai Y, He Q, Han Q, Duan S, (2012) Solid-phase extraction of trace metal ions with magnetic nanoparticles modified with 2,6-diaminopyridine. Microchimica Acta, 178:405–412. doi: 10.1007/s00604-012-0857-7

Zhao D, Guo X, Wang T, Alvarez N, Shanov VN, Heineman WR, (2014) Simultaneous Detection of Heavy Metals by Anodic Stripping Voltammetry Using Carbon Nanotube Thread. Electroanalysis, 26:488 – 496. doi: 10.1002/elan.201300511

Zhu L, Xu L, Huang B, Jia N, Tan L, Yao S, (2014) Simultaneous determination of Cd (II) and Pb (II) using square wave anodic stripping voltammetry at a gold nanoparticle-graphene-cysteine composite modified bismuth film electrode. Electrochimica Acta, 115:471– 477. doi.org/10.1016/j.electacta.2013.10.209